ACS OMEGA

Open Access

http://pubs.acs.org/journal/acsodf

Article

The N-Glycoproteomic Landscape of the Lung in Monocrotaline-Induced Pulmonary Arterial Hypertension

Guili Lian, Mohammad Ismail Hajary Sagor, Kexin Cai, Zhihai Chen, Changsheng Xu, Huajun Wang, Wei Zhuang,* Li Luo,* and Liangdi Xie*

Cite This: *ACS Omega* 2026, 11, 34404−34419

Read Online

ACCESS | Metrics & More | Article Recommendations | Supporting Information

ABSTRACT: Protein N-glycosylation plays critical roles in controlling cell function, yet its specific contributions to pulmonary arterial hypertension (PAH) remain poorly understood. Here, we performed an integrated proteomic and site-specific N-glycoproteomic analysis of lung tissues from a monocrotaline-induced PAH rat model. Using quantitative LC-MS/MS with glycoprotein enrichment, we identified 7,048 proteins in the proteome, including 1,302 differentially expressed proteins and 1,918 N-glycosylation sites across 764 glycoproteins in the N-glycoproteome. 320 glycosylation sites (from 260 glycoproteins) showed significant dysregulation. Glycoproteomic motif analysis confirmed the canonical N-X-S/T sequon, with enriched localization in plasma membrane and extracellular proteins. Bioinformatics revealed ribosome-related pathways were significantly downregulated, whereas lysosomal pathways were upregulated. Key N-glycoproteomic alterations involved integrin binding, ECM−receptor interaction, and ferroptosis. Integrated multiomics analysis of 7,136 proteome and 2,897 N-glycoproteome proteins identified 805 overlapping candidates, of which 387 exhibited concordant upregulation in lysosome, TGF-β signaling, and mineral absorption pathways. We confirmed that VCAM1 and AMBP were increased in the lungs of PAH rats by Western blot and immunofluorescence. Our study provides the first system-wide view of the N-glycoproteomic landscape of the lung in monocrotaline-induced PAH rats, revealing the involvement of N-glycosylation in ECM dysfunction, adhesion pathways, and lysosomal dysregulation, and suggests novel glycoprotein-centered targets for therapeutic intervention.

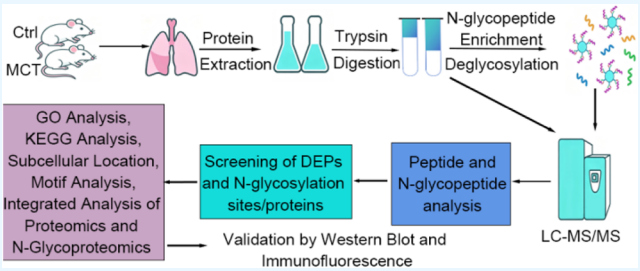

INTRODUCTION

Pulmonary arterial hypertension (PAH) is a progressive disease characterized by pulmonary vascular remodeling and sustained elevation of pulmonary arterial pressure, ultimately leading to right heart failure and death.[1,2] Despite available therapies, the prognosis of PAH patients remains poor, with a 5-year survival rate of approximately 65%.[3] Currently, clinical drugs for PAH mainly target three classical pathophysiological pathways, including prostacyclin (PGI2), endothelin-1 (ET-1), and nitric oxide (NO) pathways. These drugs exert pulmonary vasodilatory effects but do little to reverse pathological vascular remodeling.[4] Thus, investigating the pathogenesis of PAH to identify new therapeutic targets is of great significance.

Despite advances in understanding the pathophysiology of PAH, the molecular mechanisms driving disease progression remain incompletely elucidated, particularly at the level of post-translational modifications (PTMs) such as N-glycosylation. Emerging evidence recognizes aberrant glycosylation as a hallmark of PAH, offering a novel perspective on its pathogenesis.[5,6] Glycosylation is a critical modification process that regulates cardio-immunometabolism by influencing protein folding, trafficking, localization, cell adhesion, signal transduction, and immune response.[7] N-Glycosylation, the most common form, involves the attachment of specific glycan residues to asparagine residues within the conserved sequon asparagine-X-serine/threonine (N-X-S/T).[8]

Accumulating clinical and experimental evidence underscores the significance of N-glycosylation. The IgG N-glycosylation profile reflects immune dysregulation and inflammatory status in PAH and chronic thromboembolic pulmonary hypertension (CTEPH) patients, suggesting its potential as a novel biomarker for risk stratification.[5,6] Li et al. reported that hypoxia-inducible factor 1α-induced two-pore channel 2 (TPC2) transcription and subsequent STT3B-dependent TPC2 glycosylation inhibit autophagic flux and aggravate PAH.[9] Experimental PAH models revealed that increased core fucosylation and FUT8 upregulation actively drive the development of PAH.[10]

Integrating proteomics and N-glycoproteomics analyses offers a powerful approach to uncover novel biomarkers and

Received: March 2, 2026
Revised: April 23, 2026
Accepted: May 20, 2026
Published: June 3, 2026

dysregulated pathways in PAH.[11−13] While specific protein N-glycosylation events have been implicated, a comprehensive, site-specific profiling of the lung N-glycoproteome in PAH remains unexplored. In this study, we identified key proteins, N-glycosylation sites, and related pathways in the lung in monocrotaline (MCT)-induced PAH by using integrated proteomics and N-glycoproteomics analyses, and confirmed the changes of some key biomarkers by Western blot. Our study provides systematic insights into the molecular mechanisms of PAH and suggests potential targets for future diagnostic and therapeutic strategies.

MATERIALS AND METHODS

Animals

Sprague−Dawley rats (male, 180−200 g) were purchased from Beijing Huafukang Biotechnology Co., Ltd. (Beijing, China). The animals were housed under a 12 h light/dark cycle, with free access to food and water. The room temperature was 22−25 °C. After 1 week of adaptation, the experimental animals were randomly divided into the control (Ctrl) group and the MCT group. The MCT-induced PAH model was established as described in our previous study.[14] The MCT group received a single intraperitoneal injection of 40 mg/kg MCT (HY-N0750, MedChemExpress, USA). The control group rats received the same volume of normal saline. Four weeks postinjection, the development of PAH was confirmed by hemodynamic measurements and morphological analysis. All animal procedures were carried out in strict accordance with recommendations from the ARRIVE Guidelines[15] and were approved by the Laboratory Animal Welfare and Ethics Committee of Fujian Medical University (Approval No. IACUC FJMU 2022-084).

Hemodynamic Measurement

Hemodynamic measurements were performed as previously described.[16] Briefly, the rats were anesthetized with sodium pentobarbital (50 mg/kg, ip), placed in a supine position, and secured. The right jugular vein was exposed via a cervical incision. A heparinized PE-50 catheter connected to a pressure transducer was inserted and advanced through the right ventricle into the pulmonary artery to measure the pulmonary artery pressure (PAP). The correct catheter position was verified by characteristic pressure waveforms. Hemodynamic signals were continuously recorded using a PowerLab system (ADInstruments, Australia), and the mean PAP (mPAP) was derived from the data using LabChart software 6.0.

Right Ventricular Hypertrophy Index (RVHI)

The animals were humanely sacrificed for cardiac tissue analysis according to our established protocol.[14] The excised hearts were carefully dissected to separate the right ventricular (RV) free wall from the combined left ventricular and interventricular septal mass (LV + S). RVHI was then calculated as the weight ratio of RV to LV + S to assess right ventricular hypertrophy.

H&E Staining

Lung tissues were fixed in 4% paraformaldehyde, dehydrated through a graded ethanol series, embedded in paraffin, and sectioned at a thickness of 4 μm. Following deparaffinization and rehydration, sections were stained with Gill's hematoxylin for 1 min and eosin Y for 1 min, then dehydrated and mounted with neutral balsam. Images were acquired using a light microscope (Nikon ECLIPSE Ci, Japan). For morphological analysis, pulmonary arterioles with an external diameter (ED) of approximately 100 μm were selected. Vascular wall thickness (WT), ED, total vascular area (TA), and luminal area (LA) were measured using IPP 6.0 software as described.[16] From these, two indices were calculated: (1) the relative wall thickness (WT% = (2 × WT/ED) × 100) and (2) the wall area percentage (WA% = ((TA − LA)/TA) × 100). These metrics allow for the systematic quantification of pulmonary arteriolar remodeling.

Immunofluorescence

Immunofluorescence was performed as previously described.[17] Formalin-fixed, paraffin-embedded lung sections (4 μm) were deparaffinized in xylene, rehydrated through a graded ethanol series (100% to 50%), and subjected to antigen retrieval in EDTA buffer (pH 9.0) at 95 °C for 20 min. After cooling to room temperature and washing with PBS, sections were blocked with 10% nonfat milk for 30 min and then incubated overnight at 4 °C with primary antibodies against α-SMA (1:800; GB13044−50, Servicebio, China), CD68 (1:200; ab318303, Abcam, UK), VCAM1 (1:200, ET1601-18, Huabio, China), and AMBP (1:1000, ER1803-35, Huabio, China). Following PBS washes, sections were incubated with species-matched Alexa Fluor-conjugated secondary antibodies (1:200) for 1 h at room temperature. Nuclei were counterstained with DAPI, and sections were mounted with an antifade mounting medium (G1407, Servicebio). Images were acquired using a confocal microscope (FV3000, Olympus, Japan) or an inverted phase-contrast fluorescence microscope (Ts2R, Nikon, Japan).

Western Blot

Protein extracts were prepared from the lower right lung lobe using RIPA buffer. The tissue was homogenized using a tissue grinder and centrifuged, and then the supernatant was collected. The protein concentration was determined by the BCA assay. Equal amounts of protein were mixed with 2× SDS loading buffer, boiled for 10 min, and separated by SDS-PAGE. The resolved proteins were then transferred to a PVDF membrane. The membrane was blocked and subsequently incubated with primary antibodies against AMBP (1:1000, ER1803-35) and VCAM1 (1:1000, ET1601-18, Huabio, China), followed by incubation with appropriate horseradish peroxidase (HRP)-conjugated secondary antibodies. Protein bands were visualized using an enhanced chemiluminescence (ECL) substrate and imaged with an iBright FL1500 imaging system (Invitrogen). The band intensities were quantified by densitometry using ImageJ software (National Institutes of Health).

Protein Extraction and Digestion

The left lobe of the lung was cryogenically ground into a fine powder using liquid nitrogen and transferred to a 5 mL centrifuge tube. The powdered tissue was lysed with four volumes of ice-cold lysis buffer (8 M urea, 1% protease inhibitor cocktail) and disrupted by sonication on ice for 3 min using a high-intensity ultrasonic processor (Sonics, USA). The lysate was centrifuged (12,000 × g, 10 min, 4 °C) to remove insoluble debris. The supernatant was collected, and its protein concentration was determined by a BCA assay. Proteins were then precipitated by adding trichloroacetic acid to a final concentration of 20% (m/v), incubated for 2 h at 4 °C, and collected by centrifugation (4,500 × g, 5 min, 4 °C). The resulting pellet was washed three times with chilled acetone, briefly air-dried, and resolubilized in 200 mM triethylamine bicarbonate with brief sonication. For digestion, proteins were first enzymatically cleaved overnight using trypsin (1:50 enzyme-to-protein ratio). Subsequently, peptides were reduced with 5 mM dithiothreitol (30 min, 56 °C) and alkylated with 11 mM iodoacetamide (15 min at room temperature in the dark). Finally, the digested peptides were purified using a Strata-X SPE column.

N-Glycopeptides Enrichment and Deglycosylation

A fraction of the tryptic peptides (200 μg) was reconstituted in 200 μL of binding/wash buffer (80% acetonitrile, 5% trifluoroacetic acid). The supernatant was transferred to the hydrophilic interaction chromatography (HILIC) column (particle size 5 μm, pore size 120 Å, Welch, USA) and enriched by centrifugation at 1000 × g for 15 min. The HILIC column was rinsed three times with the binding/wash buffer. To improve glycopeptide recovery, the bound glycopeptides were eluted twice consecutively from the same column using 0.1% trifluoroacetic acid, 50 mM ammonium bicarbonate solution, and 50% acetonitrile, respectively. For each elution step, a fresh portion of the respective elution buffer was applied, and the two eluates were collected separately and then pooled. The pooled eluates were dried under vacuum centrifugation. After drying, the samples were reconstituted in 50 μL of 50 mM ammonium bicarbonate buffer prepared in ^{18}O-labeled water,

https://doi.org/10.1021/acsomega.6c02324
ACS Omega 2026, 11, 34404−34419

and 2 μL of PNGase F was added, followed by overnight enzymatic digestion at 37 °C. Finally, the samples were desalted according to manufacturer's instruction of the C18 ZipTip, , and subjected to LC-MS/MS analysis.

LC-MS/MS Analysis and Data Search

The LC-MS/MS analysis was conducted by Jingjie PTM BioLab Co., Inc. (Hangzhou, China). For protein analysis, the tryptic peptides were dissolved in solvent A (0.1% formic acid and 2% acetonitrile in water) and loaded onto a homemade reversed-phase analytical column with an integrated spray tip (100 μm i.d. × 25 cm) packed with 1.9 μm/120 Å ReproSil-Pu rC18 resins (Dr. Maisch GmbH, Ammerbuch, Germany). The mobile phase consisted of solvent A and solvent B (0.1% formic acid in acetonitrile). Peptides were separated with the following gradient: 0−14 min, 6−24% B; 14−16 min, 24−35% B; 16−18 min, 35−80% B; 18−20 min, 80% B; and all at a constant flow rate of 500 nL/min. The eluted peptides were subjected to a capillary source followed by the timsTOF Pro mass spectrometer (Bruker Daltonics, Germany). The electrospray voltage of 1.75 kV was applied. The mass spectrometer was operated in data-independent parallel accumulation serial fragmentation (DIA-PASEF) mode. The full MS scan was set to 300−1500 (MS/MS scan range), and 20 PASEF (MS/MS mode)-MS/MS scans were acquired per cycle. The MS/MS scan range was set to 400−850 and the isolation window was set to 7 m/z.

For N-glycopeptide LC-MS/MS analysis, the peptides were reconstituted in mobile phase A and separated using a NanoElute ultrahigh-performance liquid chromatography (UHPLC) system. Mobile phase A consisted of water containing 0.1% formic acid and 2% acetonitrile, while mobile phase B was acetonitrile/water (v/v) with 0.1% formic acid. The separation was carried out at a flow rate of 450 nL/min with the following gradient: 2−22% B over 0−16 min, 22−35% B over 16−22 min, 35−90% B over 22−26 min, and held at 90% B for 26−30 min. The eluted peptides were ionized using a Capillary ion source and analyzed on a timsTOF Pro mass spectrometer (Bruker Daltonics, Germany). The ion source voltage was set to 1.7 kV. Both MS and MS/MS spectra were acquired using TOF detection. Data acquisition was performed in DIA-PASEF mode. The MS scan ranged from 100 to 1700 m/z. For each cycle, one full MS scan was followed by 22 PASEF MS/MS scans, with the m/z range for MS/MS set to 395−1395 and a window width of 20 m/z.

DIA data were searched using Spectronaut (v 18) with default parameters. The enzyme specificity was set to trypsin/P, allowing for up to two missed cleavages. Carbamidomethylation of cysteine (Cys) was set as a fixed modification. Variable modifications included oxidation of methionine, acetylation of the protein N-terminus, and deamidation (^{18}O) of asparagine (with a mass shift of 2.99 Da), as described previously.[18] Site localization of glycopeptides is confirmed based on MS2 fragmentation spectra, and the PTM sites are listed in Table S1. Specifically, the presence of a +2.99 Da mass shift on asparagine-containing fragment ions was used to determine whether a given site was modified by N-glycosylation. The quantification of glycoproteins was normalized by using proteomics data for N-glycoproteomics analysis. A decoy database was included to estimate the false discovery rate (FDR) resulting from random matches. The FDR thresholds for protein, peptide, and peptide-spectrum-match (PSM) identification were all set to 1%.

Identification of the Differentially Expressed Proteins (DEPs) and Differentially Expressed N-Glycosylated Sites

To evaluate the reproducibility of biological replicates, principal component analysis (PCA) was performed, and the relative standard deviation (RSD) was calculated. By transforming high-dimensional protein expression data into principal components (PCs), the first two PCs (PC1 and PC2) were plotted to evaluate global patterns across sample groups. RSD was calculated as the standard deviation divided by the mean of replicated samples and was expressed as a percentage. In label-free quantitative proteomics, an RSD of <20% is commonly accepted as indicative of good reproducibility. The fold change was calculated as the ratio of the mean $\log_2$-transformed relative protein abundances between MCT and Ctrl groups. To assess statistical significance, an independent two-sample t-test was performed. Differentially expressed proteins (DEPs) and differentially N-glycosylated sites with a fold change ≥1.5 and a p value <0.05 were considered significantly upregulated, while those with a fold change ≤1/1.5 (i.e., ≤ 0.67) and a p value <0.05 were considered significantly downregulated.

Gene Ontology (GO) and Kyoto Encyclopedia of Genes and Genomes (KEGG) Annotation

Gene Ontology (GO) analysis was performed to functionally characterize the identified proteins. This analysis categorizes proteins into three primary domains: biological process (BP), molecular function (MF), and cellular component (CC).[19] The GO annotation process was conducted using the eggNOG-mapper software against the EggNOG database to assign GO terms to the identified proteins, followed by a functional classification analysis across the three domains.[20] Kyoto Encyclopedia of Genes and Genomes (KEGG) pathway analysis was employed to interpret the functional roles of proteins within metabolic and signal transduction pathways.[21] KEGG integrates knowledge on pathways, genes, compounds, and reactions. Pathway annotation was performed by comparing the protein sequences against the KEGG database using BLAST (blastp, E-value ≤1×10^{-4}).[22] For each sequence, the top-scoring hit was used to assign the KEGG pathway annotation.

Subcellular Localization Annotation

In eukaryotic cellular systems, proteins exhibit distinct distribution patterns across various intracellular compartments because of their differential affinity for membrane structures. The principal subcellular compartments in eukaryotes encompass the extracellular matrix (ECM), cytoplasm, nucleus, mitochondria, Golgi apparatus, endoplasmic reticulum, peroxisome, vesicle, cytoskeleton, nucleoplasm, nuclear matrix, and ribosome. For our analysis, we employed the WoLF PSORT computational tool to predict and annotate the spatial distribution patterns of the target proteins within these cellular compartments.

Motif Analysis

Motif patterns surrounding N-glycosylation sites were investigated using MoMo software, which utilizes the Motif-X algorithm.[23] The analysis was performed on 10-amino-acid peptide sequences flanking each glycosylation site, with all protein sequences in the database serving as the background. A statistically significant motif was defined as one that met the following two criteria: contained at least 20 peptide occurrences and achieved a p value threshold below 0.000001. Statistical significance was calculated by comparing the observed frequency of the motif in the N-glycosylated peptides against its expected frequency in the background database using the following formula: (number of glycosylated peptides containing the motif/total glycosylated peptides)/(number of database sequences containing the motif/total N-glycosylation-containing sequences in the database).

Integrated Analysis of Proteomics and N-Glycoproteomics

Integrated analysis of proteomics and N-glycoproteomics was performed using the PTMcloud tools at https://www.pt,m-biolab-css.com.cn/cloud/cloudTool. An intersection analysis was performed on the proteins identified by both the proteome and unnormalized N-glycoproteome, and the distribution of quantitative values was compared between modified and unmodified proteins. DEPs and differentially N-glycosylated sites were screened based on the previously defined criteria in this study, and a nine-quadrant plot was used to perform correlation analysis on the differential lists from the two omics. According to the threshold status of each protein at both the protein abundance level and the N-glycosylation level, all proteins were classified into nine different categories. KEGG pathway enrichment analysis and GO functional analysis were then performed for the proteins in each category. Enrichment analysis was conducted using Fisher's exact test, with fold enrichment >1.5 and $p < 0.05$ as the criteria for significant enrichment.

https://doi.org/10.1021/acsomega.6c02324
ACS Omega 2026, 11, 34404−34419

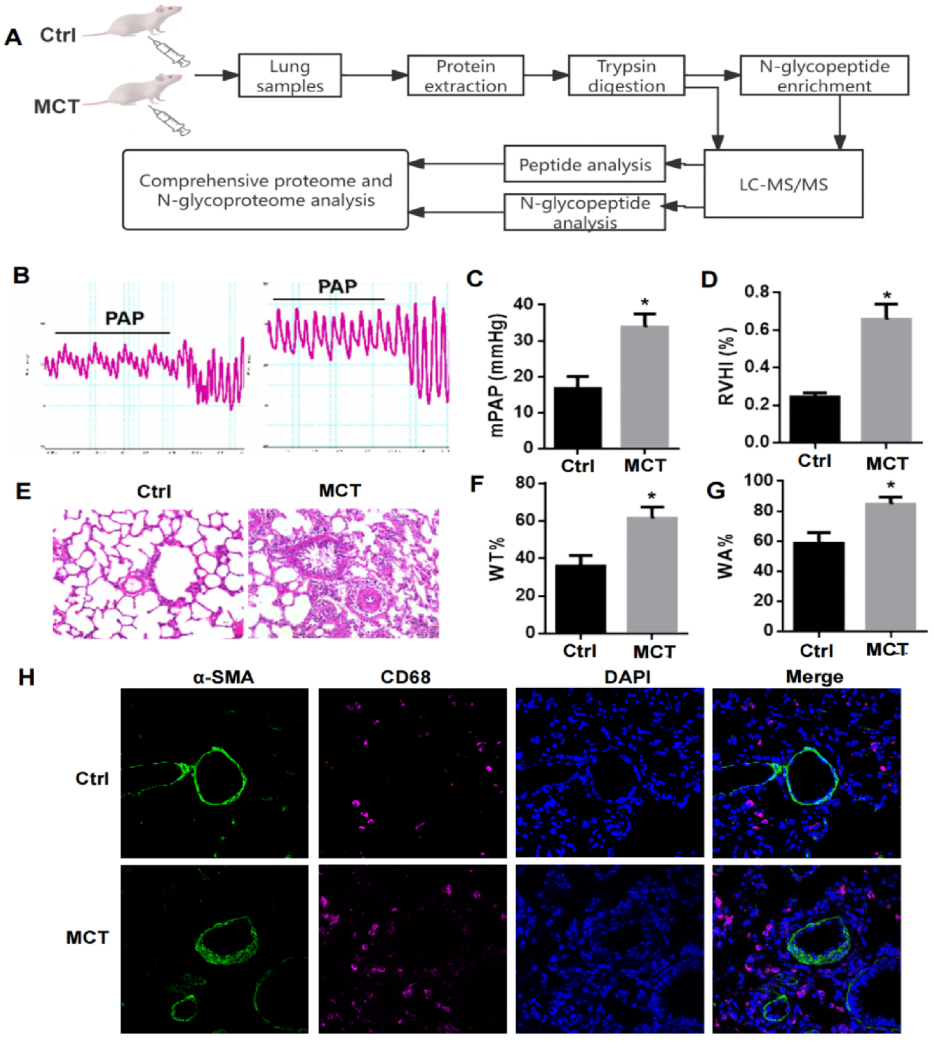

Figure 1. The flowchart of this study and the validation of MCT-induced PAH rat model. A: The flowchart of the study. B: The typical waveform of pulmonary arterial pressure in MCT-induced PAH rats and control (Ctrl) rats. C−D: The mPAP and RVHI of PAH and control rats. E: H&E staining of lung tissues in PAH rats and controls. F−G. The WT% and WA% of PAH and control rats. H: The results of α-SMA (green), CD68 (purple), and DAPI (blue) staining in PAH lungs at ×400 magnification. The data were expressed as mean ± SD (n = 8); *p < 0.05 vs Ctrl.

Statistical Analysis

The data were expressed as mean ± standard deviation (SD), and the comparisons between two groups were performed using t-test, with p < 0.05 considered statistically significant.

RESULTS

Validation of MCT-Induced PAH Rat Model

After 4 weeks of MCT injection, the lung tissues were collected. A label-free quantitative proteomics and N-glycoproteomics strategy was applied to quantify the differences in proteins and N-glycosylation between MCT and Ctrl (Figure 1A). After treatment with MCT, the mPAP and RVHI of PAH rats were higher than those of Ctrl (Figure 1B−D). It was demonstrated that the pulmonary arteries of PAH rats were significantly remodeled by H&E staining (Figure 1E). The WT% and WA% of pulmonary arteries were increased in PAH rats, as compared to control rats (Figure 1F−G). α-SMA and CD68 immunofluorescence showed that the medial layer of pulmonary arteries was thickened, and more $CD68^+$ macrophages were infiltrated in the lungs of PAH rats (Figure 1H). These results indicated that the rat model of PAH was successfully established.

The DEPs of the Proteomics Profiles in the Lungs of PAH Rats

In the present study, we performed 4D Fast DIA quantitative proteomics and bioinformatics analysis of the proteome in the lungs derived from MCT-induced PAH rats. To evaluate the reproducibility of biological replicates, we performed PCA and calculated the RSD. Our data demonstrated a clear segregation between MCT and Ctrl by PCA (Figure 2A), while the low RSD values further confirmed high reproducibility across replicates (Figure 2B). These analyses collectively indicated robust experimental consistency. DEPs with a fold change ≥1.5 and p < 0.05 were considered significantly upregulated, while those with a fold change ≤ 1/1.5 (i.e., ≤ 0.67) and p < 0.05 were considered significantly downregulated. A total of 7048 compared proteins were quantified in the proteomics analysis (Table S2), of which 1302 were identified as DEPs. Among these, 406 proteins were upregulated, and 896 were downregulated (Figure 2C and Table S3). The volcano plot and hierarchical clustering heatmap are shown in Figure 2D and E. The top 5 upregulated proteins were tryptase alpha/beta 1 (Tpsab1), Von Willebrand factor (Vwf), mast cell protease 1 (Mcpt1), carboxypeptidase A3 (Cpa3), and vitamin K epoxide

https://doi.org/10.1021/acsomega.6c02324
ACS Omega 2026, 11, 34404−34419

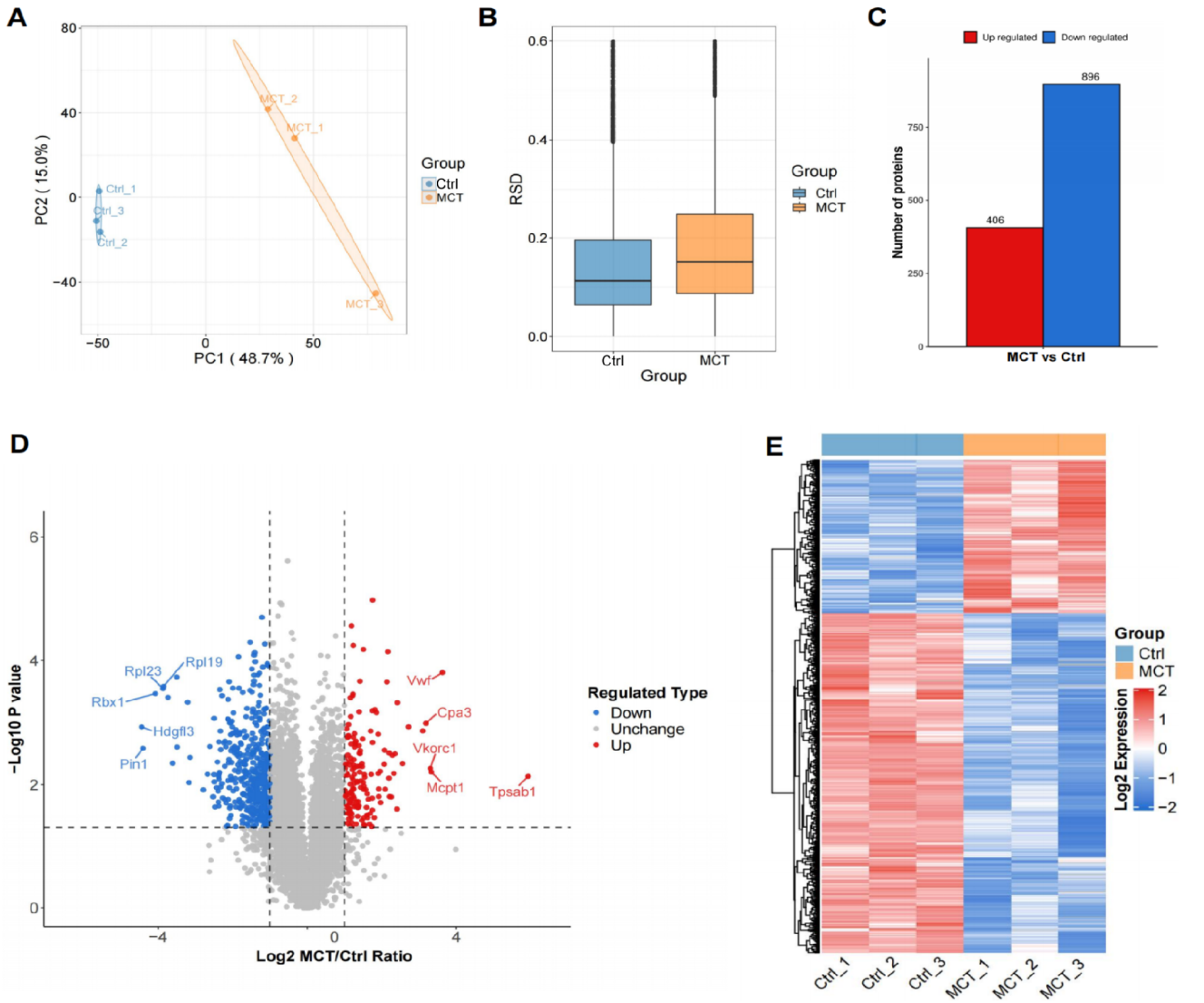

Figure 2. The proteomics analysis of lungs in PAH rats. A: The PCA plot of proteomics data of MCT and Ctrl rats. B: The RSD plot of proteomics data of MCT and Ctrl rats. C: 406 proteins were upregulated and 896 were downregulated in PAH rats. D: The volcano plot was generated to visualize differential expression analysis between MCT and Ctrl groups, incorporating *p*-values. The *x*-axis represents the Log2-transformed fold change (Ratio) values, while the *y*-axis shows the −Log10-transformed *p*-values from statistical tests. In the plot, red dots indicate significantly upregulated proteins, blue dots denote significantly downregulated proteins, and gray dots represent nonsignificant differences. The top 5 downregulated and upregulated proteins were marked in the volcano plot. E: The union set of differentially expressed proteins (DEPs) (detected in ≥2/3 samples across all comparisons) was subjected to hierarchical clustering analysis. Relative protein expression was visualized by a heatmap (red: high; blue: low; gray: missing values), with rows representing DEPs and columns representing samples.

reductase complex subunit 1 (Vkorc1), and the top 5 downregulated proteins were hemoglobin subunit delta-1-like 3 (Hgdf13), peptidyl-prolyl cis−trans isomerase NIMA-interacting 1 (Pin1), RING-box protein 1 (Rbx1), 60S ribosomal protein L23 (Rpl23), and 60S ribosomal protein L19 (Rpl19) (Figure 2D).

KEGG and GO Enrichment Analysis of Proteomics Data in PAH Lungs

The bioinformatics analysis revealed significant enrichment of DEPs in key pathways and functional categories, as demonstrated by the KEGG and GO analyses. GO analysis showed predominant enrichment in BP, such as cotranslational protein targeting to the membrane and SRP-dependent cotranslational protein targeting to the membrane. MF categories were significantly enriched for cytosolic ribosome, cell surface, and lysosomal lumen, while CC analysis highlighted the structural constituent of ribosome and serine-type peptidase activity as the most significantly represented (Figure 3A). KEGG pathway enrichment identified the top significantly altered pathways, including ribosome, protein digestion and absorption, lysosome, neuroactive ligand−receptor interaction, and ferroptosis (Figure 3B). Separate GO and KEGG enrichment analyses were performed for the upregulated and downregulated DEPs. The results showed that upregulated DEPs were mainly enriched in the regulation of acute inflammatory response (BP, Figure S1A), extracellular region (CC, Figure S1B), serine-type peptidase activity (MF, Figure S1C), and the lysosome pathway (KEGG, Figure S1D). In contrast, downregulated proteins were predominantly enriched in cotranslational protein targeting to the membrane (BP, Figure S2A), cytosolic ribosome (CC, Figure S2B), structural constituent of ribosome (MF, Figure S2C), and the ribosome pathway (KEGG, Figure S2D). The

https://doi.org/10.1021/acsomega.6c02324
ACS Omega 2026, 11, 34404−34419

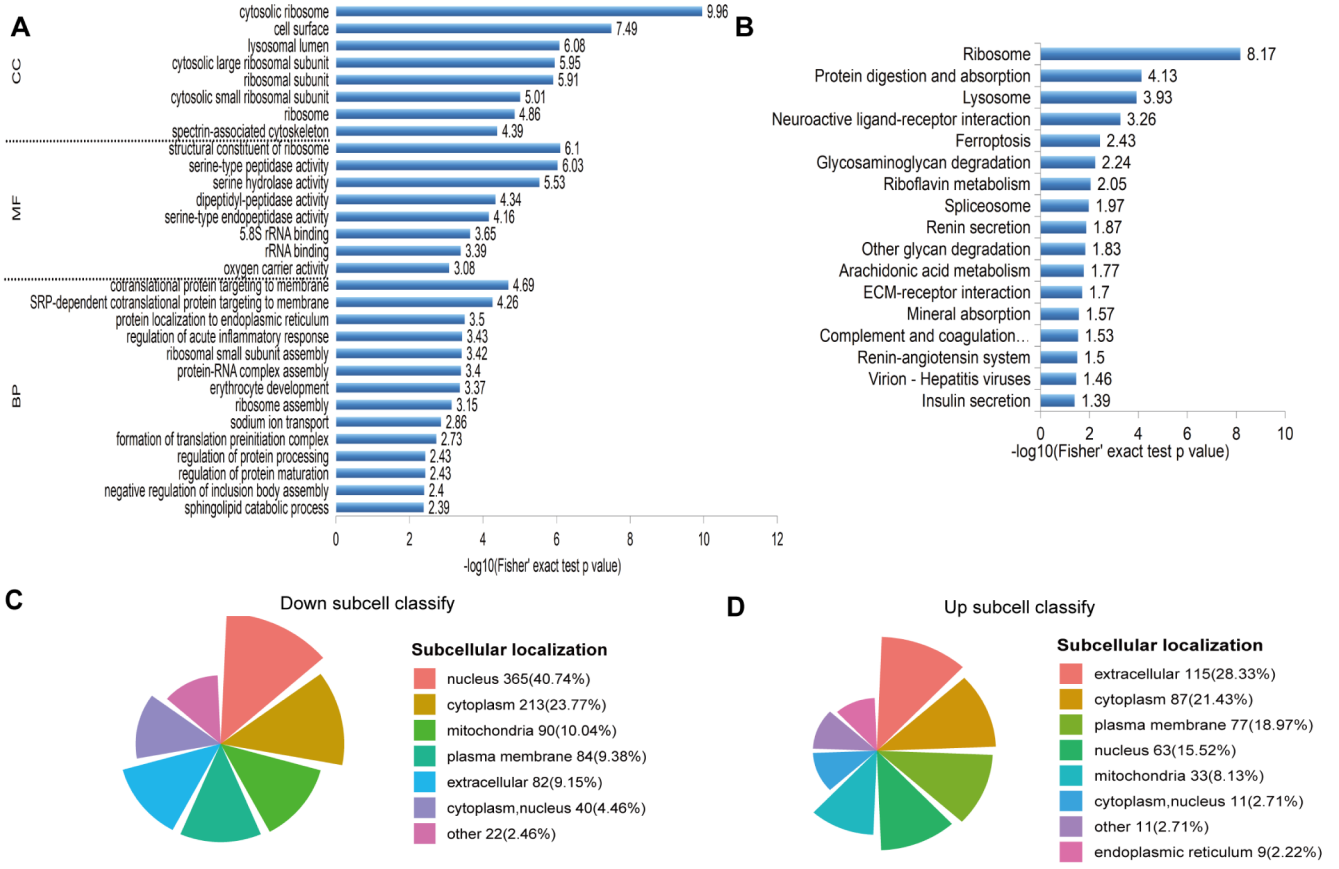

Figure 3. Bioinformatics analysis of DEPs in PAH rats. A: GO enrichment analysis of DEPs, including biological processes (BP), cellular components (CC), and molecular functions (MF). B: KEGG pathway enrichment of DEPs. C: Subcellular location of the downregulated DEPs. D: Subcellular location of the upregulated DEPs.

GO enrichment results for both upregulated and downregulated DEPs are shown in Table S4, and the KEGG enrichment results are shown in Table S5. As shown in Figure 3C−D, subcellular localization analysis revealed that the downregulated DEPs were primarily distributed in the nucleus (40.74%) and cytoplasm (23.77%), whereas the upregulated DEPs were mainly distributed in the extracellular compartment (28.33%), cytoplasm (21.43%), and plasma membrane (18.97%). The heatmap and the constituents of ribosome and lysosome are shown in Figure 4A−D. The results revealed that the subunits of the ribosome were decreased and proteins involved in the lysosome were increased in PAH rats.

N-Glycoproteomics Profile of Lungs in PAH Rats

To understand the N-glycosylation profile of lungs in PAH, we performed 4D fast DIA quantitative N-glycoproteomics and bioinformatics analysis on lungs derived from MCT-induced PAH rats. PCA revealed distinct clustering of biological replicates (PC1: 42.2%; PC2: 19.9%), with low RSD, demonstrating high reproducibility (Figure 5A−B). A total of 764 comparable proteins and 1918 comparable sites were identified in the N-glycoproteomics analysis (Figure 5C, Table S6), of which 195 N-glycosylated sites related to 158 proteins were upregulated, and 125 N-glycosylated sites associated with 102 proteins were downregulated (Figure 5D, Table S7). The volcano plot highlighted the top 5 upregulated N-glycosylation sites and the top 5 downregulated sites (Figure 5D). The heatmap of differentially expressed N-glycosylated sites is shown in Figure 5E. The top 5 upregulated N-glycosylated sites were N-acetyl-alpha-glucosaminidase (Naglu) N501, activin receptor type-1-like (Acvrl1) N32, fibrillin 1 (Fbn1) N1370, peroxidasin (Pxdn) N728, and CD46 molecule (Cr1l) N331, and the top 5 downregulated proteins were protein O-glucosyltransferase (Poglut1) N435, tetraspanin-13 (Tspan13) N113, vWF N1766, vacuolar protein sorting 25 homologue (Ramp2) N92, and tenascin-X N100 (Figure 5E).

Systematic Analysis of N-Glycosylation Features and Functional Pathways in PAH Lungs

As shown in Figure 6A−B, N-glycosylation sequence motif analysis revealed that the most significantly enriched motif was the classical N-glycosylation motif N-X-S and N-X-T, and nonclassical motif N-X-C. Bioinformatic analysis of differentially expressed N-glycoproteins revealed significant functional clustering, with GO analysis demonstrating predominant enrichment in BP, including cell−substrate junction assembly, positive regulation of neutrophil degranulation, and positive regulation of neutrophil activation. MF was dominated by integrin binding, D-mannose binding, and pantetheine hydrolase activity, while CC highlighted the integrin complex, basement membrane, and protein complex involved in cell adhesion (Figure 6C). KEGG enrichment analysis showed that ECM−receptor interaction, focal adhesion, lysosome, and ferroptosis may play a mechanistic role in linking N-glycosylation alterations to the pathogenesis of PAH (Figure 6D). Subcellular localization analysis revealed that the differentially expressed N-glycoproteins were primarily distributed in the plasma membrane and extracellular compartment, followed

https://doi.org/10.1021/acsomega.6c02324
ACS Omega 2026, 11, 34404−34419

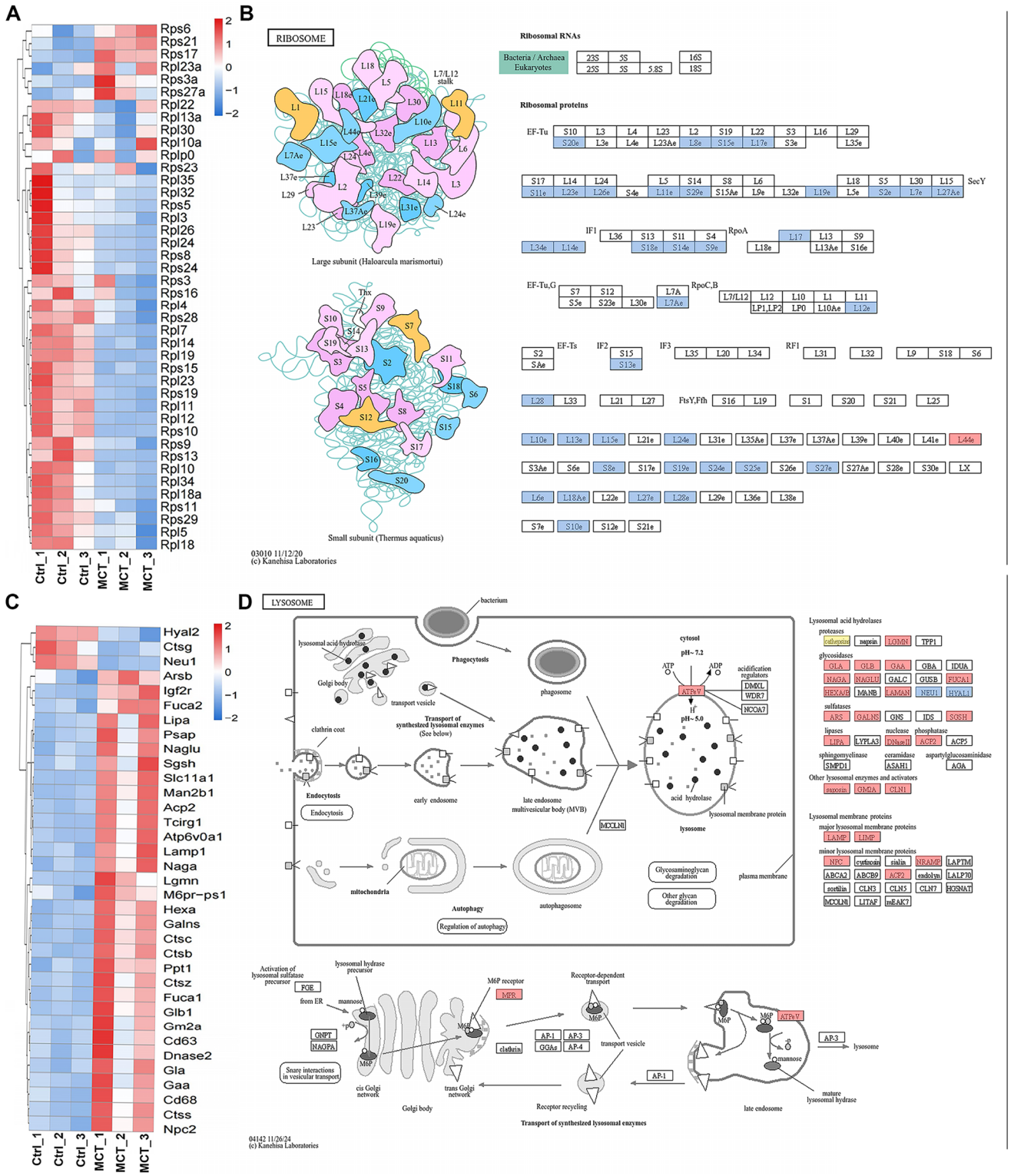

Figure 4. Ribosomal and lysosomal protein alterations in PAH rats. A: Heatmap of ribosome-related proteins, demonstrating a decrease in ribosomal subunits in PAH rats compared to controls. B: The upregulated proteins (red) and downregulated proteins (blue) in the ribosome subunits by KEGG. C: Heatmap of lysosome-related proteins, showing an increase in lysosomal proteins in PAH rats. D: The upregulated proteins (red) and downregulated proteins (blue) in the lysosome pathway of KEGG.

by cytoplasmic and endoplasmic reticulum localizations (Figure 6E).

Integrated Proteomics and N-Glycoproteomics Profiling

The plot displayed the differences in intensity ranges between the global proteome and N-glycosylated proteins. The count of the N-glycoproteomics proteins was lower than that of the corresponding proteins found in the proteomics data (Figure 7A). Quantitative analysis detected 7,136 total proteins and 2,897 N-glycosylated proteins, with 805 overlapping proteins (Figure 7B, Table S8). Nine-quadrant analysis revealed

https://doi.org/10.1021/acsomega.6c02324
ACS Omega 2026, 11, 34404−34419

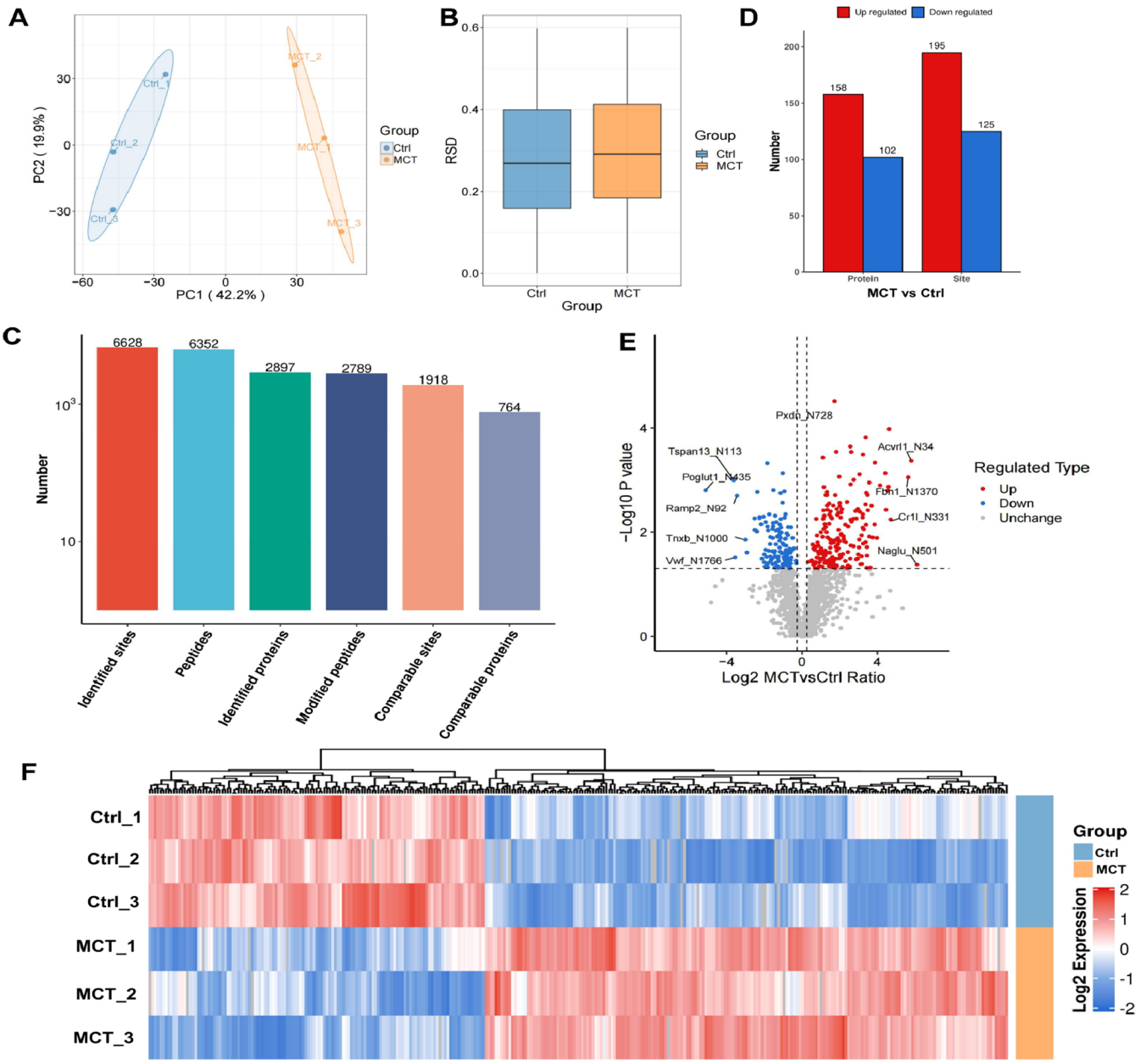

Figure 5. Quantitative N-glycoproteomics profiling of lung tissues in MCT-induced PAH rats. A: Principal component analysis (PCA) of N-glycoproteome data showing distinct clustering of biological replicates. B: Relative standard deviation (RSD) analysis demonstrating high reproducibility across replicates. C: Bar plot of identified and quantifiable items, including identified sites, peptides, identified proteins, modified peptides, comparable sites, and comparable proteins. Identified sites: Number of modification sites detected by spectrum search analysis; Peptides: Number of peptides to which the spectrum hit; Identified proteins: Number of proteins detected by spectrum search analysis; Modified peptides: Total number of modified peptides identified; Comparable sites: Number of modification sites comparable; Comparable proteins: Number of proteins comparable. D: Bar plot summarizing differentially regulated N-glycosylation proteins and sites. E: Volcano plot of N-glycosylation site alterations, highlighting the top 5 upregulated (red) and downregulated (blue) sites. F: Heatmap of significantly altered N-glycosylated proteins with hierarchical clustering showing distinct expression patterns between PAH and control groups.

concordantly upregulated proteins, downregulated proteins, and discordant targets showing opposite regulation trends (Figure 7C, Table S9). KEGG pathway enrichment analysis revealed that the significantly coupregulated pathways (both protein expression and N-glycosylation levels increased) mainly included lysosome, protein digestion and absorption, and ferroptosis. The proteins involved in the lysosomal pathway include Man2b1, Cd63, Cd68, Arsb, Naglu, Psap, Ctsc, Igf2r, Lgmn, Acp2, and Fuca1. These molecules are predominantly enriched in the lysosomal lumen and membrane structures, further confirming the significant enrichment of the lysosomal pathway in both omics data sets (Figure S3). The significantly codownregulated pathways mainly included fluid shear stress and atherosclerosis, Ras signaling pathway, and tight junction. The pathways with unchanged protein expression but upregulated N-glycosylation were mainly enriched in ECM−receptor interaction, Parkinson's disease, and the p53 signaling pathway (Figure 7D and Table S10). The heatmaps of GO functional enrichment results (BP, CC, MF) for proteome and N-glycoproteome are shown in Figure S3.

https://doi.org/10.1021/acsomega.6c02324
ACS Omega 2026, 11, 34404−34419

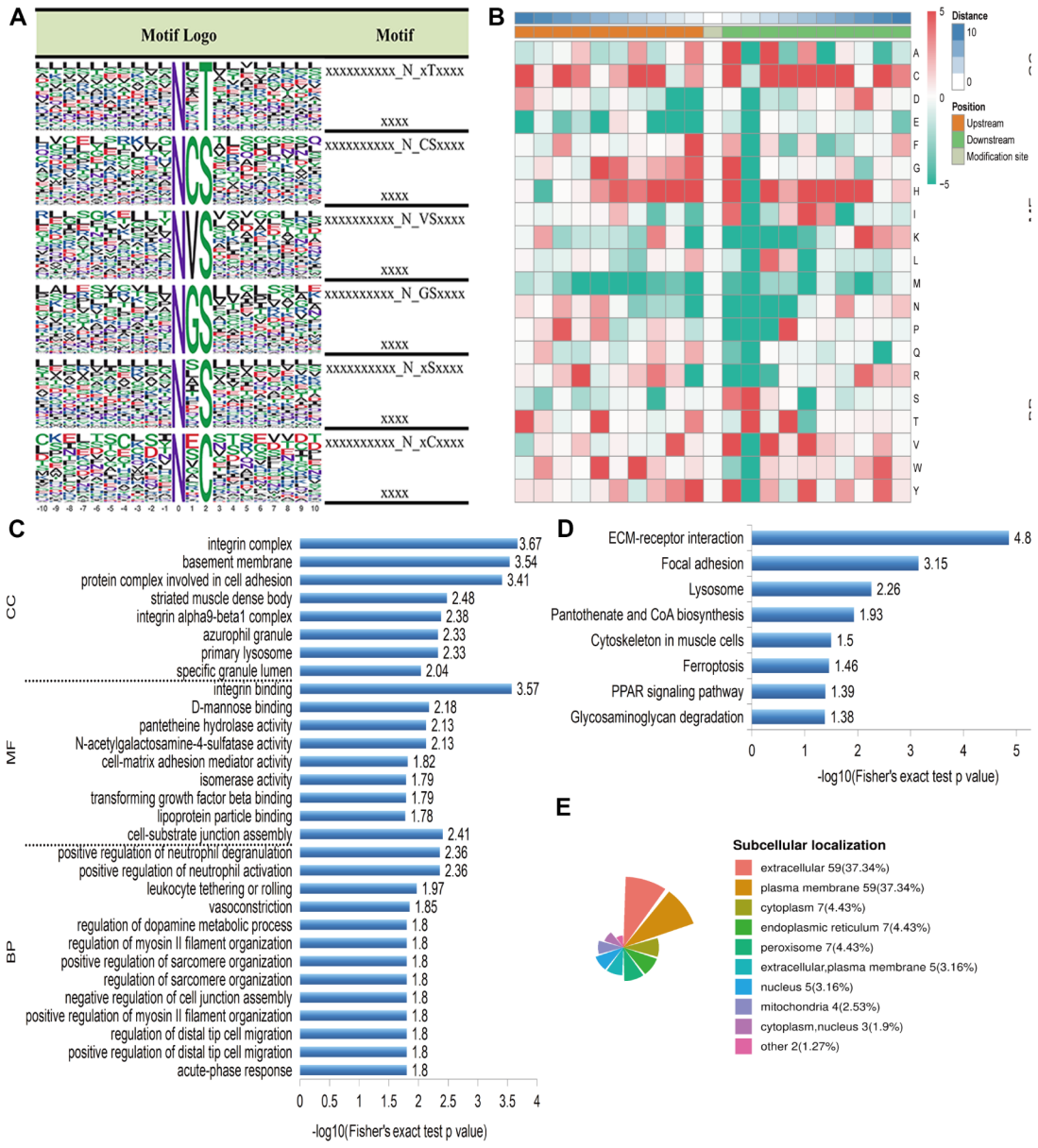

Figure 6. Systematic analysis of N-glycosylation features and functional pathways in PAH lungs. A: Sequence logo of N-glycosylation motifs. B: The heatmap displays Z-score normalized log-transformed *p* values for each amino acid at positions from −10 to +10 relative to the N-glycosylation site (position 0). The color scale ranges from −5 to +5 after normalization. Red represents a higher occurrence frequency of the amino acid at the corresponding position (enrichment), while green represents a lower occurrence frequency (depletion). C: GO enrichment analysis of differentially expressed N-glycoproteins across biological processes (BP), molecular functions (MF), and cellular components (CC). D: KEGG pathway enrichment analysis identifying key pathways potentially linking N-glycosylation to PAH pathogenesis. E: Subcellular localization analysis of differentially expressed N-glycoproteins, demonstrating predominant plasma membrane and extracellular distribution, followed by cytoplasmic and endoplasmic reticulum localization.

Validation of VCAM1 and AMBP Expression in PAH

Our integrated proteomic and N-glycoproteomic analyses revealed a significant dysregulation of protein expression and N-glycosylation in the lungs of MCT-induced PAH rats. The nine-quadrant analysis identified 60 proteins that were significantly upregulated at the total protein level, concurrently accompanied by the upregulation of 101 specific N-glycosylation sites (Figure 7C and Table S9). From this data set, two candidates, vascular cell adhesion molecule 1 (VCAM1) and alpha-1-microglobulin/bikunin precursor (AMBP), were selected for biological validation based on their significant upregulation at both the protein and glycosylation levels. The Western blot analysis confirmed these omics findings at both the total protein and the site-specific glycosylation levels. The glycosylation occupancy at site N423 of VCAM1 and site N233 of AMBP was significantly increased in PAH lung tissues (Figure 8A−D). Consistent with this, the total protein expression levels of both VCAM1 and AMBP were also significantly elevated in the MCT-induced PAH group compared with controls by Western blot (Figure 8E−G) and immunofluorescence (Figure 8H−I). As shown in Figure 8H−I, VCAM1 expression was weakly expressed in the lung tissue of control rats but was significantly upregulated in pulmonary arterial endothelial cells after MCT treatment, whereas AMBP was widely expressed in the lung tissues.

https://doi.org/10.1021/acsomega.6c02324
ACS Omega 2026, 11, 34404−34419

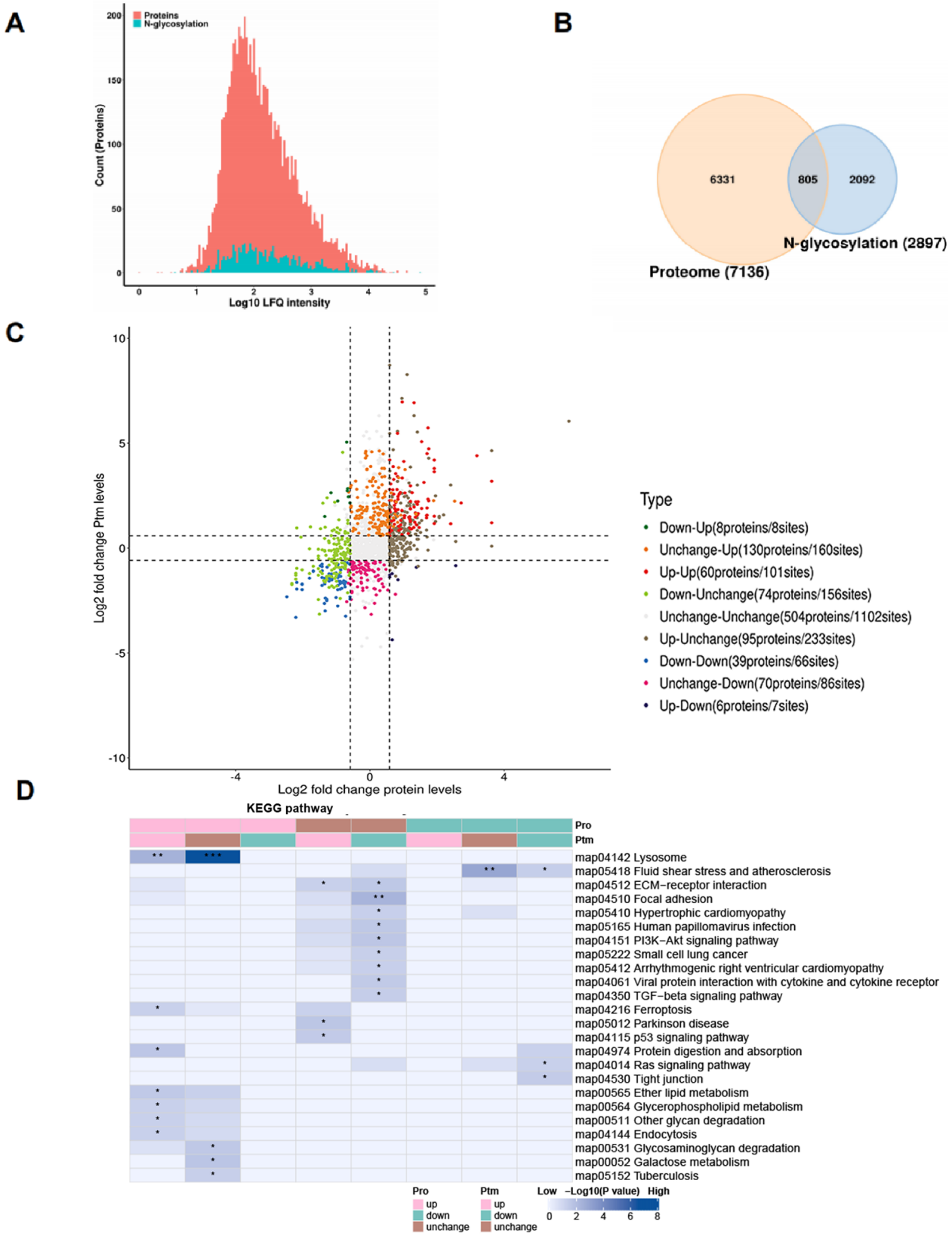

Figure 7. Quantitative profiling and pathway analysis of N-glycosylated proteins in PAH. A: The histogram displays the intensity distribution of all quantified proteins (red) and N-glycosylated proteins (blue) after Log10 transformation. The *x*-axis represents Log10-transformed protein intensity values, and the *y*-axis indicates the counts of corresponding proteins. B: Venn diagram displaying 7,136 total identified proteins (gray), 2,897 N-glycosylated proteins (blue), and their 805 overlapping targets. C: Nine-quadrant regulation analysis of N-glycosylated proteins. D: KEGG pathway enrichment analysis of the integrated proteomic and N-glycoproteomic profiles. Each column represents a protein-modification association category, and each row represents a significantly enriched functional term. The color intensity of each block indicates the significance level of functional

https://doi.org/10.1021/acsomega.6c02324
ACS Omega 2026, 11, 34404−34419

Figure 7. continued

enrichment, with darker colors representing higher significance. Asterisks denote the degree of significant enrichment: *$p < 0.05$, **$p < 0.01$, ***$p < 0.001$.

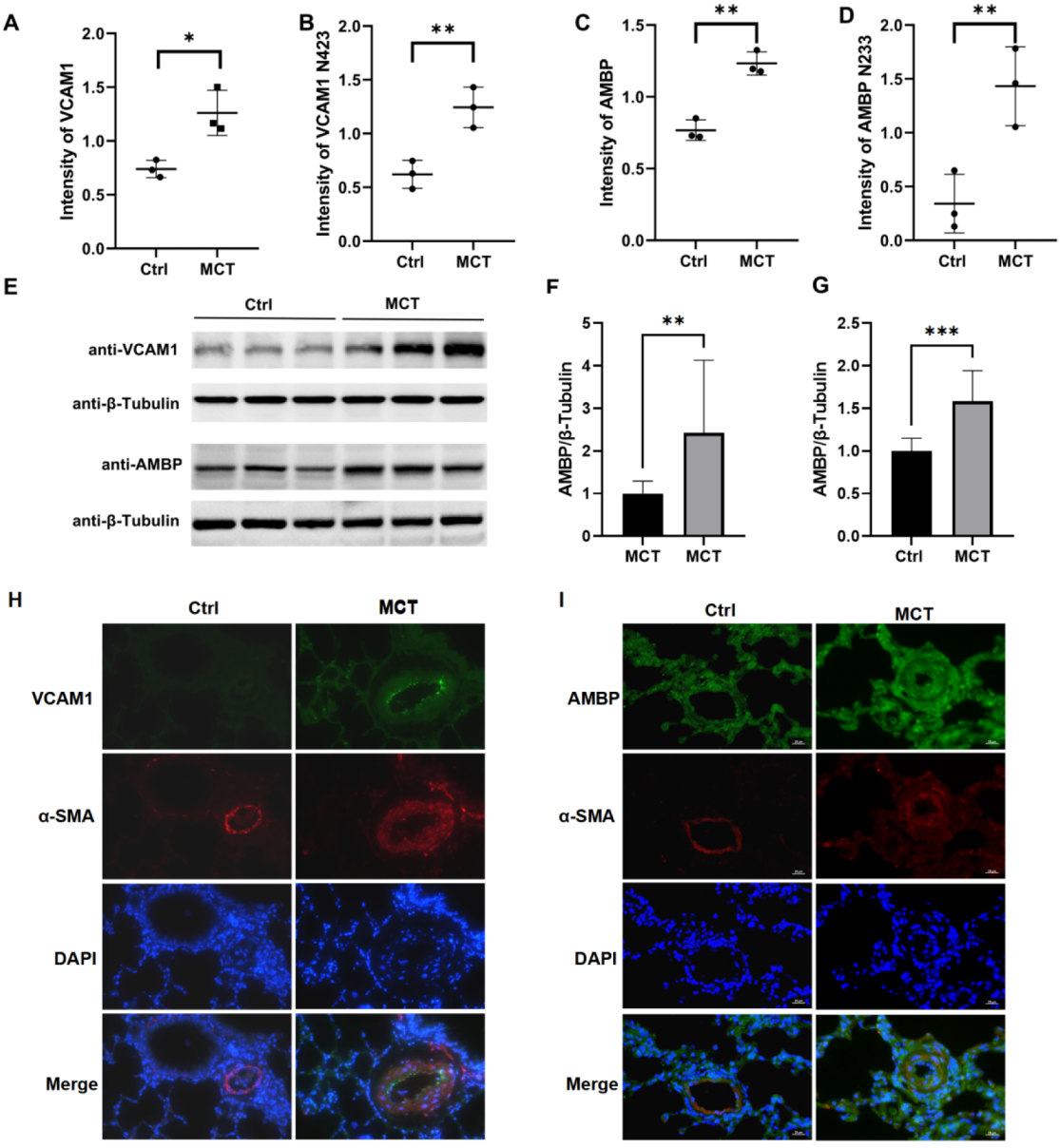

Figure 8. Elevation of VCAM1 and AMBP in lungs of MCT-induced PAH rats. A−B: Proteomic and N-glycoproteomic analyses revealed an increase in total protein level and N423-site glycosylation of VCAM1 in MCT-treated rats. C−D: Total protein level and N233-site glycosylation of AMBP were elevated in MCT-treated rats. E: Representative Western blot images showing protein expression of VCAM1 and AMBP in lung tissues. F−G: Quantitative analysis of VCAM1 and AMBP protein levels. H−I: Immunofluorescence results of VCAM1 and AMBP expression in lung tissues. Representative images show α-SMA (red), VCAM1 (green, H) or AMBP (green, I), DAPI (blue), and the merged channels (Merge) at ×400 magnification. Data are presented as mean ± SD; $n = 10$ (Ctrl), $n = 8$ (MCT); *$p < 0.05$, **$p < 0.01$, ***$p < 0.001$ vs Ctrl.

DISCUSSION

Several recent omics studies have investigated molecular changes in PAH. Luo et al.[2] performed quantitative proteomic and phosphoproteomic profiling of lung tissues from a PAH rat model, identifying numerous DEPs and phosphorylation sites. Meanwhile, Zhang et al.[5,6] reported that plasma IgG N-glycome traits have prognostic value in both PAH and CTEPH patients, revealing a proinflammatory IgG glycosylation phenotype. While these studies provide valuable insights into protein abundance, signaling phosphorylation, and circulating glycan biomarkers, none have examined site-specific N-glycosylation in lung tissues from any PAH animal model.

This study presents the first comprehensive integrated proteomics and N-glycoproteomics analyses of lung tissues in MCT-induced PAH, revealing significant dysregulation of ribosomal (downregulated) and lysosomal (upregulated) pathways in PAH, along with altered N-glycosylation patterns, particularly in ECM and adhesion-related proteins. Integrated

https://doi.org/10.1021/acsomega.6c02324
ACS Omega 2026, 11, 34404−34419

proteomics and N-glycoproteomics data revealed overlapping upregulated pathways: lysosome, TGF-β signaling, and mineral absorption. The findings highlight ribosomal/lysosomal imbalance and N-glycosylation-mediated ECM/adhesion alterations as key pathological mechanisms, suggesting lysosomal pathways and adhesion glycoproteins as potential therapeutic targets.

The MCT-induced PAH rat model is a well-established model of group I pulmonary hypertension. Consistent with our previous studies,[14,16] it was demonstrated that elevated mPAP, RVHI, WT%, and WA% exists in this model. Immunofluorescence further confirmed medial wall thickening (α-SMA$^+$) and increased infiltration of CD68$^+$ macrophages, aligning with solid evidence of inflammatory involvement in PAH.[16,24,25] These findings collectively validate the model's ability to recapitulate key features of human PAH, including vascular remodeling and inflammation.

Proteomics profiling of MCT-induced PAH rat lungs identified 1,302 proteins DEPs (406 upregulated and 896 downregulated). The top upregulated proteins included Tpsab1 and Mcpt1 (mast cell-associated proteases), Vwf (endothelial dysfunction marker), Cpa3 (inflammatory mediator), and Vkorc1 (vitamin K metabolism), suggesting prominent roles for mast cell activation, vascular injury, and coagulation pathways in PAH pathogenesis. Conversely, downregulated proteins such as Hgdf13 (hemoglobin-related), Pin1 (cell-cycle regulator), Rbx1 (ubiquitination), and ribosomal proteins (Rpl23/Rpl19) indicate impaired oxygen sensing, proliferative suppression, and translational dysregulation. These findings align with prior studies showing that mast cells promote vascular remodeling,[26,27] and targeting endothelial dysfunction via Vwf improves outcomes for patients with PAH.[28] Notably, the observed decreases in ribosomal subunits represent a novel finding that has not been previously reported in PAH. Overall, the proteomics signature underscores the interplay between inflammatory, vascular, and metabolic disturbances and nominates new candidates including Hgdf13, Rbx1, and ribosomal proteins for future functional validation.

Bioinformatic analysis highlighted pronounced dysregulation of ribosomal and lysosomal pathways in MCT-induced PAH. Downregulation of ribosomal subunits aligns with inhibited translation pathways observed in PAH. In contrast, upregulation of lysosomal proteins (e.g., Lamp1, Ctsc, Ctsb, Ctss, Ctsz) suggests lysosomal activation, consistent with findings that lysosome-associated proteins promote the development of PAH.[29,30] These opposing trends—suppressed ribosomal function and enhanced lysosomal activity may reflect compensatory cellular stress responses to MCT-induced vascular injury, where impaired protein synthesis coexists with increased proteolytic clearance of damaged components. Additionally, pathway enrichment analysis underscored roles for ferroptosis and neuroactive ligand−receptor pathways, reinforcing the multifactorial metabolic and signaling disruptions in PAH. The link between ferroptosis and PAH, recently described by Kazmirczak et al.[31] further supports the relevance of our findings. Together, these data highlight ribosome and lysosome dysregulation as central features of PAH, potentially contributing to vascular remodeling via altered protein homeostasis and cell survival.

The N-glycoproteomic analysis of lungs from MCT-induced PAH rats revealed significant alterations in N-glycosylation patterns. Increased N-glycosylation was observed at Naglu (N501), Acvrl1 (N32), and Fbn1 (N1370). Acvrl1 is a critical mediator of bone morphogenetic protein signaling,[32] and its dysregulation is implicated in PAH. The increased glycosylation of Fbn1, an ECM protein,[33] may be associated with vascular remodeling in PAH. The downregulation of Vwf and Tenascin-X N-glycosylation may further reflect perturbations in coagulation and ECM homeostasis during PAH progression.[34,35] This comprehensive N-glycosylation profile provides novel insights into the molecular mechanisms underlying PAH.

Our results further suggest that N-glycosylation modifications may play a critical role in the pathogenesis of PAH through ECM−receptor interactions and focal adhesion pathways. Bioinformatics localization revealed that differentially expressed N-glycoproteins were primarily localized to the plasma membrane and ECM, consistent with their roles in cell-ECM communication and vascular remodeling in PAH.[36,37] KEGG pathway enrichment analysis demonstrated significant activation of ECM−receptor interaction and focal adhesion pathways, providing new insights into how glycosylation modifications participate in PAH vascular remodeling. Experimental evidence has shown that targeting ECM remodeling is crucial,[38] while the enrichment of integrin-binding functions observed in this study further supports the central role of ECM−receptor interactions in PAH. At the molecular level, N-glycosylation modifications may contribute to PAH progression by regulating the functions of integrin complexes. Previous work indicated that N-glycosylation changes in ECM proteins within vascular smooth muscle cells can influence vascular integrity, which aligns with the basement-membrane-component enrichment found in this study. Furthermore, a more in-depth study reveals that FUT8-mediated core fucosylation can promote pulmonary vascular remodeling in PAH by modulating VEGFR signaling,[10] and our GO analysis showed enrichment of neutrophil activation-related pathways, suggesting that glycosylation may simultaneously participate in the cross-regulation of inflammatory responses and vascular remodeling.[39] These findings provide novel perspectives for understanding the molecular mechanisms of PAH.

The disparity between the total proteome (7,136 proteins) and the N-glycoproteome (2,897 proteins) underscores the selectivity of protein N-glycosylation. The lower count of N-glycosylated proteins compared to the total proteome suggests that glycosylation is a regulated post-translational modification targeting specific protein subsets rather than a universal feature.[40] The 805 overlapping proteins represent core glycoproteins that maintain essential functions across cellular systems. The nine-quadrant analysis revealing 387 concordantly upregulated and 292 downregulated glycoproteins indicates coordinated regulation of the N-glycoproteome during biological processes.[41] KEGG pathway enrichment of coupregulated proteins in lysosomal functions, viral infection pathways (hepatitis viruses), TGF-β signaling, and mineral absorption aligns with known roles of glycoproteins in host−pathogen interactions, cellular signaling, and ion homeostasis.[42] The molecular function enrichment in carbohydrate binding (monosaccharide/D-mannose binding) reflects the structural role of glycans in molecular recognition.[43] The discordant regulation observed in 126 proteins (quadrants III/VII) may reflect context-dependent glycosylation changes or technical limitations in glycoproteome quantification. We selected VCAM1 and AMBP for further validation. In consistency with the results of proteomics and N-glycoproteomics, the protein levels of VCAM1 and AMBP were increased in the lungs of PAH rats. VCAM1, also known as vascular adhesion molecule, plays a

https://doi.org/10.1021/acsomega.6c02324
ACS Omega 2026, 11, 34404−34419

significant role in the pathogenesis of PAH by mediating immune cell−cell interactions and promoting vascular inflammation, which contributes to pathological vascular remodeling. Studies have shown that VCAM1 expression is upregulated in vascular smooth muscle cells under inflammatory conditions, enhancing macrophage adhesion and perpetuating inflammatory responses in the pulmonary vasculature.[44] Additionally, elevated levels of VCAM1 are associated with accelerated endothelial-mesenchymal transition (EMT) and inflammation.[45] The involvement of VCAM1 in EMT, inflammation, and vascular remodeling underscores its potential as a therapeutic target in PAH. AMBP is a multifunctional protein involved in inflammatory regulation, antioxidant activity, and extracellular proteolysis. It has demonstrated protective effects in kidney injury models by scavenging radicals and binding free heme groups.[46] In cardiovascular contexts, AMBP overexpression was shown to reduce aortic valve calcification and fibrosis in high-cholesterol diet-induced models, while its knockdown promoted osteogenic differentiation and calcium deposition.[47] Although direct evidence in PAH remains limited, AMBP's association with inflammatory resolution and its regulatory role in vascular calcification pathways suggest potential relevance in PAH pathogenesis, particularly given the shared features of vascular remodeling and inflammation.

Several limitations must be acknowledged in this study. First, the sample size was small (n = 3 per group), which may limit statistical power and generalizability. Second, clustering of the MCT group samples was suboptimal in both proteomics and N-glycoproteomics data with relatively high RSD values. This may be attributable to individual biological variation among MCT-treated rats, as well as increased technical variability introduced by the enrichment and deglycosylation steps inherent to the N-glycoproteomics workflow. Third, the present study did not experimentally validate the N-glycosylation status of the identified glycoproteins. Fourth, no mechanistic experiments were performed to validate the functional roles of the candidate genes (e.g., VCAM1 and AMBP) in the PAH pathogenesis. Future studies with larger sample sizes, optimized protocols, and mechanistic approaches are needed to further confirm our findings and improve data reproducibility.

CONCLUSION

This study represents the first comprehensive integrated analysis of proteomics and N-glycoproteomics in PAH lung tissues, revealing significant dysregulation in ribosomal and lysosomal pathways, and N-glycosylation-mediated ECM interactions that contribute to PAH pathogenesis. Our N-glycoproteome findings highlight the critical regulatory role of N-glycosylation in cell adhesion and ECM−receptor interactions, with experimental validation demonstrating the elevated expression of VCAM1 and AMBP in PAH lung tissues.

The identification of lysosomal pathways and adhesion-related N-glycoproteins as potential therapeutic targets aligns with the current advancements in glycoproteomics-based biomarker discovery. Future investigations should prioritize (1) validation of these targets in preclinical models and (2) assessment of their clinical relevance through glycoproteomics profiling of patient-derived samples. To fully understand the functional consequences of N-glycosylation in disease progression, further development of N-glycan analysis techniques is essential. This study establishes a foundation for understanding glycosylation-mediated mechanisms in PAH pathogenesis and identifies promising directions for future therapeutic developments.

ASSOCIATED CONTENT

Data Availability Statement

The mass spectrometry proteomics and N-glycoproteomics data have been deposited to the ProteomeXchange Consortium (https://proteomecentral.proteomexchange.org) via the iProX partner repository[48,49] with the data set identifier PXD068643 with the password (P042). The data that support the findings of this study are available from the corresponding author upon reasonable request.

Supporting Information

The Supporting Information is available free of charge at https://pubs.acs.org/doi/10.1021/acsomega.6c02324.

Figures S1−S3 (PDF)
Table S1: Summary of PTM sites confirmed by MS2 fragmentation spectra (XLSX)
Table S2: Proteomic profiles of lungs in MCT-induced PAH rats and controls (XLSX)
Table S3: List of 406 upregulated proteins in PAH and 896 downregulated proteins in PAH (XLSX)
Table S4: GO enrichment results for upregulated and downregulated DEPs (XLSX)
Table S5: KEGG enrichment analysis for upregulated and downregulated DEPs (XLSX)
Table S6: N-glycoproteomic profiles (including normalized data) of lung tissues from MCT-induced PAH rats and control rats (XLSX)
Table S7: List of 195 upregulated N-glycosylated sites related to 158 proteins and 125 downregulated N-glycosylated sites associated with 102 proteins in PAH (XLSX)
Table S8: Identification of overlapping proteins between proteomics and N-glycoproteomics in PAH (XLSX)
Table S9: Detailed information on differential intersection analysis between proteomics and N-glycoproteomics (XLSX)
Table S10: KEGG pathway enrichment analysis results with involved gene lists by integrated analysis of proteomics and N-glycoproteomics (XLSX)

AUTHOR INFORMATION

Corresponding Authors

Liangdi Xie − *Department of Geriatrics, the First Affiliated Hospital and Fujian Hypertension Research Institute, the First Affiliated Hospital, Fujian Medical University, Fuzhou 350005, China; Department of Geriatrics, National Regional Medical Center, Binhai Campus of the First Affiliated Hospital and Branch of National Clinical Research Center for Aging and Medicine, the First Affiliated Hospital, Fujian Medical University, Fuzhou 350212, China; Clinical Research Center for Geriatric Hypertension Disease of Fujian Province, the First Affiliated Hospital, Fujian Medical University, Fuzhou 350005, China;* orcid.org/0000-0001-5544-3149; Email: ldxield@163.com

Li Luo − *Department of Geriatrics, the First Affiliated Hospital and Fujian Hypertension Research Institute, the First Affiliated Hospital, Fujian Medical University, Fuzhou 350005, China; Department of Geriatrics, National Regional Medical Center, Binhai Campus of the First Affiliated Hospital and Branch of*

https://doi.org/10.1021/acsomega.6c02324
ACS Omega 2026, 11, 34404−34419

National Clinical Research Center for Aging and Medicine, the First Affiliated Hospital, Fujian Medical University, Fuzhou 350212, China; Clinical Research Center for Geriatric Hypertension Disease of Fujian Province, the First Affiliated Hospital, Fujian Medical University, Fuzhou 350005, China; Email: hluoli@126.com

Wei Zhuang − *Fujian Hypertension Research Institute, the First Affiliated Hospital, Fujian Medical University, Fuzhou 350005, China; Department of Cardiology, the First Affiliated Hospital, Fujian Medical University, Fuzhou 350005, China; Department of Cardiology, National Regional Medical Center, Binhai Campus of the First Affiliated Hospital, Fujian Medical University, Fuzhou 350212, China*; Email: zwfy006@163.com

Authors

Guili Lian − *Department of Geriatrics, the First Affiliated Hospital and Fujian Hypertension Research Institute, the First Affiliated Hospital, Fujian Medical University, Fuzhou 350005, China; Department of Geriatrics, National Regional Medical Center, Binhai Campus of the First Affiliated Hospital and Branch of National Clinical Research Center for Aging and Medicine, the First Affiliated Hospital, Fujian Medical University, Fuzhou 350212, China; Clinical Research Center for Geriatric Hypertension Disease of Fujian Province, the First Affiliated Hospital, Fujian Medical University, Fuzhou 350005, China*

Mohammad Ismail Hajary Sagor − *Department of Geriatrics, the First Affiliated Hospital and Fujian Hypertension Research Institute, the First Affiliated Hospital, Fujian Medical University, Fuzhou 350005, China; Department of Geriatrics, National Regional Medical Center, Binhai Campus of the First Affiliated Hospital and Branch of National Clinical Research Center for Aging and Medicine, the First Affiliated Hospital, Fujian Medical University, Fuzhou 350212, China; Clinical Research Center for Geriatric Hypertension Disease of Fujian Province, the First Affiliated Hospital, Fujian Medical University, Fuzhou 350005, China*

Kexin Cai − *Department of Geriatrics, the First Affiliated Hospital and Fujian Hypertension Research Institute, the First Affiliated Hospital, Fujian Medical University, Fuzhou 350005, China; Department of Geriatrics, National Regional Medical Center, Binhai Campus of the First Affiliated Hospital and Branch of National Clinical Research Center for Aging and Medicine, the First Affiliated Hospital, Fujian Medical University, Fuzhou 350212, China; Clinical Research Center for Geriatric Hypertension Disease of Fujian Province, the First Affiliated Hospital, Fujian Medical University, Fuzhou 350005, China*

Zhihai Chen − *Department of Geriatrics, the First Affiliated Hospital and Fujian Hypertension Research Institute, the First Affiliated Hospital, Fujian Medical University, Fuzhou 350005, China; Department of Geriatrics, National Regional Medical Center, Binhai Campus of the First Affiliated Hospital and Branch of National Clinical Research Center for Aging and Medicine, the First Affiliated Hospital, Fujian Medical University, Fuzhou 350212, China; Clinical Research Center for Geriatric Hypertension Disease of Fujian Province, the First Affiliated Hospital, Fujian Medical University, Fuzhou 350005, China*

Changsheng Xu − *Department of Geriatrics, the First Affiliated Hospital and Fujian Hypertension Research Institute, the First Affiliated Hospital, Fujian Medical University, Fuzhou 350005, China; Department of Geriatrics, National Regional Medical Center, Binhai Campus of the First Affiliated Hospital and Branch of National Clinical Research Center for Aging and Medicine, the First Affiliated Hospital, Fujian Medical University, Fuzhou 350212, China; Clinical Research Center for Geriatric Hypertension Disease of Fujian Province, the First Affiliated Hospital, Fujian Medical University, Fuzhou 350005, China*

Huajun Wang − *Department of Geriatrics, the First Affiliated Hospital and Fujian Hypertension Research Institute, the First Affiliated Hospital, Fujian Medical University, Fuzhou 350005, China; Department of Geriatrics, National Regional Medical Center, Binhai Campus of the First Affiliated Hospital and Branch of National Clinical Research Center for Aging and Medicine, the First Affiliated Hospital, Fujian Medical University, Fuzhou 350212, China; Clinical Research Center for Geriatric Hypertension Disease of Fujian Province, the First Affiliated Hospital, Fujian Medical University, Fuzhou 350005, China*

Complete contact information is available at: https://pubs.acs.org/10.1021/acsomega.6c02324

Author Contributions

L.X., L.L., W.Z., and G.L. conceptualization; G.L, M.I.H.S., and K.C. data curation; G.L., M.I.H.S., K.C., and Z.C. formal analysis; G.L. and W.Z. funding acquisition; G.L., M.I.H.S., and Z.C. investigation; G.L. and M.I.H.S. methodology; H.W. and G.L. project administration; G.L., L.X., and L.L. resources; G.L. software; C.X. supervision; G.L. visualization; G.L. and M.I.H.S. writing—original draft; L.X., G. L., M.I.H.S., K.C., Z.C., C.X., H.W., W.Z., and L.L. writing—review and editing. G.L. and M.I.H.S. contributed equally.

Funding

This work was supported by the project grants from Fujian Provincial Natural Science Foundation (2024J01526), Joint Funds for the Innovation of Science and Technology, Fujian Province (2023Y9045 and 2021Y9143), Fujian Provincial Health Science and Technology Project (2024GGA029), and National Natural Science Foundation of China (81700267).

Notes

The authors declare no competing financial interest.

■ ACKNOWLEDGMENTS

We thank Jingjie PTM BioLab (HangZhou) Co., Inc. for the LC-MS/MS analysis and technical support.

■ REFERENCES

(1) Wang, G.; Wang, Z. Investigation into the role of H2-Ab1 in vascular remodeling in pulmonary arterial hypertension via Bioinformatics. *BMC Pulm. Med.* **2024**, *24* (1), 342.

(2) Luo, A.; Jia, Y.; Hao, R.; Yu, Y.; Zhou, X.; Gu, C.; Ren, M.; Tang, H. Quantitative Proteomic and Phosphoproteomic Profiling of Lung Tissues from Pulmonary Arterial Hypertension Rat Model. *Int. J. Mol. Sci.* **2023**, *24* (11), 9629.

(3) Papadopoulos, G. E.; Arvanitaki, A.; Markidis, E.; Mouratoglou, S. A.; Farmakis, I. T.; Gourgiotis, P.; Chrysochoidis Trantas, T.; Feloukidis, C.; Kouparanis, A.; Didagelos, M.; Grosomanidis, V.; Ziakas, A.; Giannakoulas, G. Temporal trends in diagnostic hemodynamics and survival of patients with pulmonary hypertension: A single-center study. *Life* **2023**, *13* (11), 2225.

(4) Sitbon, O.; Boucly, A.; Weatherald, J.; Antigny, F.; Guignabert, C.; Jevnikar, M.; Jais, X.; Price, L. C.; Wilkins, M. R.; Zamanian, R. T.;

Savale, L.; Montani, D.; Humbert, M. Drugs targeting novel pathways in pulmonary arterial hypertension. *Eur. Respir. J.* **2025**, *66* (2), 2401830.
(5) Zhang, Z. J.; Liu, C.; Ma, J. L.; Ma, J. S.; Wang, J.; Li, R. N.; Lu, D.; Zhou, Y. P.; Lian, T. Y.; Zhang, S. J.; Li, J. H.; Wang, L.; Sun, K.; Cheng, C. Y.; Wu, W. H.; Jiang, X.; Jing, Z. C. Prognostic Value of Plasma Immunoglobulin G N-Glycome Traits in Pulmonary Arterial Hypertension. *J. Am. Coll. Cardiol.* **2024**, *84* (12), 1092−1103.
(6) Zhang, Z. J.; Wang, H. F.; Lian, T. Y.; Zhou, Y. P.; Xu, X. Q.; Guo, F.; Wei, Y. P.; Li, J. Y.; Sun, K.; Liu, C.; Pan, L. R.; Ren, M.; Nie, L.; Dai, H. L.; Jing, Z. C. Human Plasma IgG N-Glycome Profiles Reveal a Proinflammatory Phenotype in Chronic Thromboembolic Pulmonary Hypertension. *Hypertension* **2023**, *80* (9), 1929−1939.
(7) Svecla, M.; Li-Gao, R.; Falck, D.; Bonacina, F. N-glycosylation signature and its relevance in cardiovascular immunometabolism. *Vasc. Pharmacol.* **2025**, *159*, 107474.
(8) Couto, P. M.; Guardia, C. M. A.; Couto, F. L.; Labriola, C. A.; Labanda, M. S.; Caramelo, J. J. Acceptors stability modulates the efficiency of post-translational protein N-glycosylation. *FASEB J.* **2024**, *38* (13), No. e23782.
(9) Li, C.; Li, C.; Jiang, Y.; Liu, M.; Yang, C.; Lu, J.; Jiang, Y. Hypoxia-induced TPC2 transcription and glycosylation aggravates pulmonary arterial hypertension by blocking autophagy flux. *Sci. Rep.* **2024**, *14* (1), 31223.
(10) Zhang, W.; Lin, W.; Zeng, X.; Zhang, M.; Chen, Q.; Tang, Y.; Sun, J.; Liang, B.; Zha, L.; Yu, Z. FUT8-Mediated Core Fucosylation Promotes the Pulmonary Vascular Remodeling in Pulmonary Arterial Hypertension. *Aging Dis.* **2023**, *14* (5), 1927−1944.
(11) Hu, X.; Song, J.; Ye, G.; Zhu, M.; Lan, J.; Zeng, L.; Ke, Z.; Yuan, J. Integrated serum proteomic and N-glycoproteomic characterization of dengue patients. *J. Med. Virol.* **2024**, *96* (7), No. e29775.
(12) Luo, M.; Mao, Y.; Zeng, W.; Zheng, S.; Li, H.; Hu, J.; Xie, X.; Zhang, Y. Site-specific N-glycosylation characterization of micro monoclonal immunoglobulins based on EThcD-sceHCD-MS/MS. *Front. Immunol.* **2022**, *13*, 1013990.
(13) Yang, L.; Meng, B.; Gong, X.; Jiang, Y.; Shentu, X.; Xue, Z. Investigation of the synergistic effect mechanism underlying sequential use of palbociclib and cisplatin through integral proteomic and glycoproteomic analysis. *Anticancer Drugs* **2024**, *35* (9), 806−816.
(14) Chen, X.; Yu, X.; Lian, G.; Tang, H.; Yan, Y.; Gao, G.; Huang, B.; Luo, L.; Xie, L. Canagliflozin inhibits PASMCs proliferation via regulating SGLT1/AMPK signaling and attenuates artery remodeling in MCT-induced pulmonary arterial hypertension. *Biomed. Pharmacother.* **2024**, *174*, 116505.
(15) Kilkenny, C.; Browne, W. J.; Cuthill, I. C.; Emerson, M.; Altman, D. G. Improving bioscience research reporting: the ARRIVE guidelines for reporting animal research. *PLoS Biol.* **2010**, *8* (6), No. e1000412.
(16) Zhuang, W.; Lian, G.; Huang, B.; Du, A.; Xiao, G.; Gong, J.; Xu, C.; Wang, H.; Xie, L. Pulmonary arterial hypertension induced by a novel method: Twice-intraperitoneal injection of monocrotaline. *Exp. Biol. Med.* **2018**, *243* (12), 995−1003.
(17) Xiao, G.; Lian, G.; Wang, T.; Chen, W.; Zhuang, W.; Luo, L.; Wang, H.; Xie, L. Zinc-mediated activation of CREB pathway in proliferation of pulmonary artery smooth muscle cells in pulmonary hypertension. *Cell Commun. Signaling* **2021**, *19* (1), 103.
(18) Tao, S.; Orlando, R. A novel method for relative quantitation of N-glycans by isotopic labeling using ^{18}O-water. *J. Biomol. Tech.* **2014**, *25* (4), 111−117.
(19) Feng, S.; Cai, K.; Lin, S.; Chen, X.; Luo, Y.; Wang, J.; Lian, G.; Lin, Z.; Xie, L. Exploring potential therapeutic agents for lipopolysaccharide-induced septic cardiomyopathy based on transcriptomics using bioinformatics. *Sci. Rep.* **2023**, *13* (1), 20589.
(20) Huerta-Cepas, J.; Forslund, K.; Coelho, L. P.; Szklarczyk, D.; Jensen, J.; von Mering, C.; Bork, P. Fast Genome-Wide Functional Annotation through Orthology Assignment by eggNOG-Mapper. *Mol. Biol. Evol.* **2017**, *34* (8), 2115−2122.
(21) Kanehisa, M.; Goto, S.; Sato, Y.; Furumichi, M.; Tanabe, M. KEGG for integration and interpretation of large-scale molecular data sets. *Nucleic Acids Res.* **2012**, *40*, D109−D114.
(22) Kanehisa, M.; Sato, Y.; Kawashima, M.; Furumichi, M.; Tanabe, M. KEGG as a reference resource for gene and protein annotation. *Nucleic Acids Res.* **2016**, *44* (D1), D457−62.
(23) Chou, M. F.; Schwartz, D. Biological sequence motif discovery using motif-x. *Curr. Protoc. Bioinf.* **2011**, *35*, 13.15.1−13.15.24.
(24) Rampa, D. R.; Murugesan, P.; Chao, H.; Feng, H.; Dai, W.; Lee, D.; Pekcec, A.; Doods, H.; Wu, D. Reversal of pulmonary arterial hypertension and neointimal formation by kinin B1 receptor blockade. *Respir. Res.* **2021**, *22* (1), 281.
(25) Savai, R.; Pullamsetti, S. S.; Kolbe, J.; Bieniek, E.; Voswinckel, R.; Fink, L.; Scheed, A.; Ritter, C.; Dahal, B. K.; Vater, A.; Klussmann, S.; Ghofrani, H. A.; Weissmann, N.; Klepetko, W.; Banat, G. A.; Seeger, W.; Grimminger, F.; Schermuly, R. T. Immune and inflammatory cell involvement in the pathology of idiopathic pulmonary arterial hypertension. *Am. J. Respir. Crit. Care Med.* **2012**, *186* (9), 897−908.
(26) Farha, S.; Sharp, J.; Asosingh, K.; Park, M.; Comhair, S. A.; Tang, W. H.; Thomas, J.; Farver, C.; Hsieh, F.; Loyd, J. E.; Erzurum, S. C. Mast cell number, phenotype, and function in human pulmonary arterial hypertension. *Pulm. Circ.* **2012**, *2* (2), 220−228.
(27) Hu, Y.; Chi, L.; Kuebler, W. M.; Goldenberg, N. M. Perivascular inflammation in pulmonary arterial hypertension. *Cells* **2020**, *9* (11), 2338.
(28) Kawut, S. M.; Horn, E. M.; Berekashvili, K. K.; Widlitz, A. C.; Rosenzweig, E. B.; Barst, R. J. von Willebrand factor independently predicts long-term survival in patients with pulmonary arterial hypertension. *Chest* **2005**, *128* (4), 2355−2362.
(29) Chang, C. J.; Hsu, H. C.; Ho, W. J.; Chang, G. J.; Pang, J. S.; Chen, W. J.; Huang, C. C.; Lai, Y. J. Cathepsin S promotes the development of pulmonary arterial hypertension. *Am. J. Physiol.: Lung Cell. Mol. Physiol.* **2019**, *317* (1), L1−l13.
(30) Peng, Z.; Luo, X. Y.; Li, X.; Li, Y.; Wu, Y.; Tian, Y.; Pan, B.; Petrovic, A.; Kosanovic, D.; Schermuly, R. T.; Ruppert, C.; Gunther, A.; Zhang, Z.; Qiu, C.; Li, Y.; Pu, J.; Li, X.; Chen, A. F. Cathepsin L Promotes Pulmonary Hypertension via BMPR2/GSDME-Mediated Pyroptosis. *Hypertension* **2024**, *81* (12), 2430−2443.
(31) Kazmirczak, F.; Vogel, N. T.; Prisco, S. Z.; Patterson, M. T.; Annis, J.; Moon, R. T.; Hartweck, L. M.; Mendelson, J. B.; Kim, M.; Calixto Mancipe, N.; Markowski, T.; Higgins, L.; Guerrero, C.; Kremer, B.; Blake, M. L.; Rhodes, C. J.; Williams, J. W.; Brittain, E. L.; Prins, K. W. Ferroptosis-Mediated Inflammation Promotes Pulmonary Hypertension. *Circ. Res.* **2024**, *135* (11), 1067−1083.
(32) Jimmidi, R.; Monsivais, D.; Ta, H. M.; Sharma, K. L.; Bohren, K. M.; Chamakuri, S.; Liao, Z.; Li, F.; Hakenjos, J. M.; Li, J.-Y.; et al. Discovery of highly potent and ALK2/ALK1 selective kinase inhibitors using DNA-encoded chemistry technology. *Proc. Natl. Acad. Sci. U. S. A.* **2024**, *121* (47), No. e2413108121.
(33) Alonso, F.; Dong, Y.; Li, L.; Jahjah, T.; Dupuy, J.-W.; Fremaux, I.; Reinhardt, D. P.; Genot, E. Fibrillin-1 regulates endothelial sprouting during angiogenesis. *Proc. Natl. Acad. Sci. U. S. A.* **2023**, *120* (23), No. e2221742120.
(34) Rabinovitch, M.; Andrew, M.; Thom, H.; Trusler, G. A.; Williams, W. G.; Rowe, R. D.; Olley, P. M. Abnormal endothelial factor VIII associated with pulmonary hypertension and congenital heart defects. *Circulation* **1987**, *76* (5), 1043−1052.
(35) Liang, G.; Wang, S.; Shao, J.; Jin, Y. J.; Xu, L.; Yan, Y.; Günther, S.; Wang, L.; Offermanns, S. Tenascin-X Mediates Flow-Induced Suppression of EndMT and Atherosclerosis. *Circ. Res.* **2022**, *130* (11), 1647−1659.
(36) Nie, X.; Shen, C.; Tan, J.; Wu, Z.; Wang, W.; Chen, Y.; Dai, Y.; Yang, X.; Ye, S.; Chen, J.; Bian, J. S. Periostin: A Potential Therapeutic Target For Pulmonary Hypertension? *Circ. Res.* **2020**, *127* (9), 1138−1152.
(37) Ambade, A. S.; Hassoun, P. M.; Damico, R. L. Basement Membrane Extracellular Matrix Proteins in Pulmonary Vascular and Right Ventricular Remodeling in Pulmonary Hypertension. *Am. J. Respir. Cell Mol. Biol.* **2021**, *65* (3), 245−258.
(38) Kucherenko, M. M.; Sang, P.; Yao, J.; Gransar, T.; Dhital, S.; Grune, J.; Simmons, S.; Michalick, L.; Wulsten, D.; Thiele, M.; et al. Elastin stabilization prevents impaired biomechanics in human

https://doi.org/10.1021/acsomega.6c02324
ACS Omega 2026, 11, 34404−34419

pulmonary arteries and pulmonary hypertension in rats with left heart disease. *Nat. Commun.* **2023**, *14* (1), 4416.
(39) Xie, X.; Kong, S.; Cao, W. Targeting protein glycosylation to regulate inflammation in the respiratory tract: Novel diagnostic and therapeutic candidates for chronic respiratory diseases. *Front. Immunol.* **2023**, *14*, 1168023.
(40) Chau, T. H.; Chernykh, A.; Kawahara, R.; Thaysen-Andersen, M. Critical considerations in N-glycoproteomics. *Curr. Opin. Chem. Biol.* **2023**, *73*, 102272.
(41) Feng, X.; Zheng, X.; Lin, A.; Yang, S.; Zhang, S.; Wu, D.; Wu, W.; Han, X. FBN1 knockout promotes cervical artery dissection by inducing N-glycosylation alternation of extracellular matrix proteins in rat VSMCs. *Cell. Signalling* **2023**, *110*, 110834.
(42) Wang, Z.; Jia, X.; Ma, J.; Zhang, Y.; Sun, Y.; Bo, X. Global profiling of the proteome, phosphoproteome, and N-glycoproteome of protoscoleces and adult worms of Echinococcus granulosus. *Front. Vet. Sci.* **2023**, *10*, 1275486.
(43) Atashi, M.; Jiang, P.; Nwaiwu, J.; Gutierrez Reyes, C. D.; Nguyen, H. M. T.; Li, Y.; Ahmadi, P.; Purba, W. T.; Mechref, Y. (15)N metabolic labeling-TMT multiplexing approach to facilitate the quantitation of glycopeptides derived from cell lines. *Anal. Bioanal. Chem.* **2024**, *416* (18), 4071−4082.
(44) Liu, H.; Jia, K.; Ren, Z.; Sun, J.; Pan, L.-L. PRMT5 critically mediates TMAO-induced inflammatory response in vascular smooth muscle cells. *Cell Death Dis.* **2022**, *13* (4), 299.
(45) Otsuki, S.; Saito, T.; Taylor, S.; Li, D.; Moonen, J.-R.; Marciano, D. P.; Harper, R. L.; Cao, A.; Wang, L.; Ariza, M. E.; et al. Monocyte-released HERV-K dUTPase engages TLR4 and MCAM causing endothelial mesenchymal transition. *JCI Insight* **2021**, *6* (15), No. e146416.
(46) Marcello, M.; Schone, L. M.; Booke, H.; Hognon-Bak, K.; Zarbock, A. Recombinant alpha-1 microglobulin to improve outcomes in survivors of AKI. *Nephrol., Dial., Transplant.* **2026**, *41*, 649−656.
(47) Guo, C.; Liu, X.; Mei, Z.; Chang, M.; Li, J.; Wang, B.; Ji, W.; Zhang, M.; Zhang, M.; Zhang, C.; An, G. AMBP protects against aortic valve calcification by inhibiting ERK1/2 and JNK pathways mediated by FHL3. *Theranostics* **2025**, *15* (10), 4398−4415.
(48) Ma, J.; Chen, T.; Wu, S.; Yang, C.; Bai, M.; Shu, K.; Li, K.; Zhang, G.; Jin, Z.; He, F.; Hermjakob, H.; Zhu, Y. iProX: an integrated proteome resource. *Nucleic Acids Res.* **2019**, *47* (D1), D1211−d1217.
(49) Chen, T.; Ma, J.; Liu, Y.; Chen, Z.; Xiao, N.; Lu, Y.; Fu, Y.; Yang, C.; Li, M.; Wu, S.; Wang, X.; Li, D.; He, F.; Hermjakob, H.; Zhu, Y. iProX in 2021: Connecting proteomics data sharing with big data. *Nucleic Acids Res.* **2022**, *50* (D1), D1522−d1527.

https://doi.org/10.1021/acsomega.6c02324
ACS Omega 2026, 11, 34404−34419